Structural Effects of Cation Size Variance in Magnetoresistive Manganese Oxide Perovskites

Lide M. Rodríguez-Martínez and J. Paul Attfield*

Department of Chemistry, University of Cambridge, Lensfield Road, Cambridge CB2 1EW, United Kingdom, and Interdisciplinary Research Centre in Superconductivity, University of Cambridge, Madingley Road, Cambridge CB3 0HE, United Kingdom

Received October 28, 1998. Revised Manuscript Received March 15, 1999

The structures of $La_{0.7}Ca_{0.11}Sr_{0.19}MnO_3$, $La_{0.32}Pr_{0.38}Sr_{0.3}MnO_3$, $Pr_{0.7}Sr_{0.23}Ba_{0.07}MnO_3$, and $Nd_{0.7}Sr_{0.16}Ba_{0.14}MnO_3$ have been refined from 4 K powder neutron diffraction data. These samples have all the same doping level and mean A cation size radius, but the A cation size variance σ^2 increases across the series. Cell parameters and coherent and incoherent atomic displacements all change systematically with σ^2. The largest changes to the MnO_3 framework are in the incoherent structure, and we conclude that these are responsible for the strong linear depression of the metal−insulator transition temperature by σ^2.

Introduction

The observation of colossal magnetoresistances (CMR) in manganese oxide perovskites of general formula $Ln_{1-x}M_xMnO_3$ (Ln = trivalent lanthanide, M = Ca, Sr or Ba) has given rise to much research to understand and improve their properties. The wide variety of electronic and magnetic states observed in these manganites can be tuned by variations in chemical composition,[1−4] external pressure,[1] temperature,[5] and magnetic field strength.[6,7] The changes in chemical composition can be described in terms of the carrier concentration (oxidation state), the tolerance factor and, as recently shown, the effect of cation size disorder. Hence quaternary $Ln_{1-x}M_xMnO_3$ systems have complex phase diagrams with different magnetic, electronic, and structural boundaries.[3]

Over certain ranges of carrier concentration, usually $0.2 \leq x \leq 0.5$, the $Ln_{1-x}M_xMnO_3$ systems exhibit a paramagnetic insulator to ferromagnetic metal transition as the temperature is decreased, giving rise to a maximum in the resistivity at a temperature T_m, which is close to the Curie temperature T_C observed by magnetization measurements. In an applied magnetic field, the resistivity drops and shifts to higher temperatures producing colossal negative magnetoresistances around T_m. The second controlling parameter, the tolerance factor, describes the effect of the average size of the A-site cations (Ln and M) on the magnetotransport properties and structure of these materials. It has been shown that a systematic decrease in the average ionic radius of the A site, $\langle r_A \rangle$, at fixed carrier concentrations, produces a decrease in T_C and a drastic increase in the magnitude of the magnetoresistance,[4] suggesting that the change of $\langle r_A \rangle$ is associated with changes in Mn−O−Mn angles, affecting the electron hopping between Mn sites. The third factor to be considered is the effect of disorder. A-site substitution, which is necessary for varying x and $\langle r_A \rangle$, usually results in size disorder or mismatch. This effect can be quantified by the variance (second moment) of the A-site cation distribution, $\sigma^2 = \langle r_A^2 \rangle - \langle r_A \rangle^2$, and we have previously shown that in a series of $Ln_{0.7}M_{0.3}MnO_3$ perovskites with constant $\langle r_A \rangle$, T_m decreases linearly with σ^2.[8] This effect was attributed to random displacements of the oxygen atoms due to the A-site disorder. This disorder effect has also been observed in $Ln_{0.5}M_{0.5}MnO_3$ perovskites[9] and in $(Ln_{1.85}M_{0.15})CuO_4$ superconductors.[10]

Structural studies have proved important in understanding the relationships between magnetotransport properties and composition.[11−13] They have demon-

(1) Hwang, H. Y.; Palstra, T. T. M.; Cheong, S.-W.; Batlogg, B. *Phys. Rev. B*. **1995**, *52*, 15046.
(2) Mahesh, R.; Mahendiran, R.; Raychaudhuri, A. K.; Rao, C. N. R. *J. Solid State Chem*. **1995**, *120*, 204. Raveau, B.; Maignan, A.; Caignaert, V. *J. Solid State Chem*. **1995**, *117*, 424. Ibarra, M. R.; Algarabel, P. A.; Marquina, C.; Blasco, J.; Garcia, J. *Phys. Rev. Lett*. **1995**, *75*, 3541.
(3) Schiffer, P.; Ramirez, A. P.; Bao, W.; Cheong, S.-W. *Phys. Rev. Lett*. **1995**, *75*, 3336.
(4) Hwang, H. Y.; Cheong, S.-W.; Radaelli, P. G.; Marezio, M.; Batlogg, B. *Phys. Rev. Lett*. **1995**, *75*, 914; Fontcuberta, J.; Martinez, B.; Seffar, A.; Pinol, S.; GarciaMunoz, J. L.; Obradors, X. *Phys. Rev. Lett*. **1996**, *76*, 1122; Maignan, A.; Simon, C.; Caignaert, V.; Raveau, B. *Zeit. Phys.* **1996**, *99*, 305.
(5) Tokura, Y.; Urushibara, A.; Moritomo, Y.; Arima, T.; Asamitsu, A.; Kido, G.; Furukawa, N. *J. Phys. Soc. Jpn*. **1994**, *63*, 3931.
(6) Asamitsu, A.; Moritomo, Y.; Tomioka, Y.; Arima, T.; Tokura, Y. *Nature* **1995**, *373*, 407.
(7) Kuwahara, H.; Tomioka, Y.; Asamitsu, A.; Moritomo, Y.; Tokura, Y. *Science* **1995**, *270*, 961.
(8) Rodriguez-Martinez, L. M.; Attfield, J. P. *Phys. Rev. B* **1996**, *54*, R15622.
(9) Damay, F.; Martin, C.; Maignan, A.; Raveau, B. *J. Appl. Phys*. **1997**, *82*, 6181.
(10) Attfield, J. P.; McAllister, J. A.; Kharlanov, A. L. *Nature* **1998**, *394*, 157.
(11) Argyriou, D. N.; Hinks, D. G.; Mitchell, J. F.; Potter, C. D.; Schultz, A. J.; Young, D. M.; Jorgensen, J. D.; Bader, S. D. *J. Solid State Chem*. **1996**, *124*, 381.
(12) Dai, P.; Zhang, J.; Mook, H. A.; Liou, S.-H.; Dowben, P. A.; Plummer, E. W. *Phys. Rev. B* **1996**, *54*, R3694.
(13) Rao, G. H.; Sun, J. R.; Liang, J. K.; Zhow, W. Y. *Phys. Rev. B* **1997**, *55*, 3742.

10.1021/cm980759y CCC: $18.00
Published on Web 05/13/1999

strated the importance of lattice distortions[14,15] and polarons or magnetopolarons[16] to the physics of these materials and have revealed the existence of new phases.[17,18] In particular, structure dependence upon composition,[19−21] $\langle r_A \rangle$,[18,22] and pressure and temperature[23] have been studied extensively, giving relationships between properties, structure and carrier concentration, and tolerance factor. In this paper, we present the first study of the effects of A-site disorder on the structure of a series of perovskites with constant doping level and mean A cation size, but variable disorder, σ^2. Four of the previously reported $Ln_{0.7}M_{0.3}MnO_3$ compositions[8] with $\langle r_A \rangle = 1.23$ Å, which show linear dependence of T_m upon σ^2, have been studied by time-of-flight neutron diffraction, and a detailed description of these results is given in this work. A preliminary account has been published elsewhere.[24]

Experimental Section

Polycrystalline $Ln_{0.7}M_{0.3}MnO_3$ oxides (10 g) were prepared under identical conditions by solid-state reaction of appropriate mixtures of oxides (La_2O_3, Pr_6O_{11}, Nd_2O_3, BaO_2, and MnO_2) and carbonates ($SrCO_3$ and $CaCO_3$) in air at 950 °C. The preheated powders were ground, pressed into pellets, sintered at 1350 °C for 10 days with several intermediate regrindings and repelletings, and finally quenched to room temperature.

The cation compositions of the samples were checked by energy dispersive analysis (EDS) of 30 microcrystallites using a JEM-2010 electron microscope. A series of standard specimens of general formula $LnMnO_3$ (Ln = La, Pr, or Nd) and $MMnO_3$ (M = Ca, Sr, or Ba) were prepared by solid-state reaction. The formal manganese oxidation state of the four samples was determined by iodometric titration under Ar atmosphere to prevent iodide oxidation by atmospheric oxygen.

Neutron time-of-flight (TOF) powder diffraction data were collected at 4 K on the POLARIS diffractometer at the ISIS source, Rutherford Appleton Laboratory (UK). Data from the low-resolution, low-angle ($14° < 2\theta < 30°$), and high-resolution, backscattering ($135° < 2\theta < 158°$) detector banks were simultaneously fitted by the Rietveld method, using the GSAS program.[25] The backscattering bank provides data down to 0.4 Å d spacings, allowing the atomic displacement factors to be refined accurately. The low-angle data contain the strong magnetic Bragg reflections at high d spacings.

Results

The EDS analyses of the four polycrystalline samples showed the cation distributions to be homogeneous.

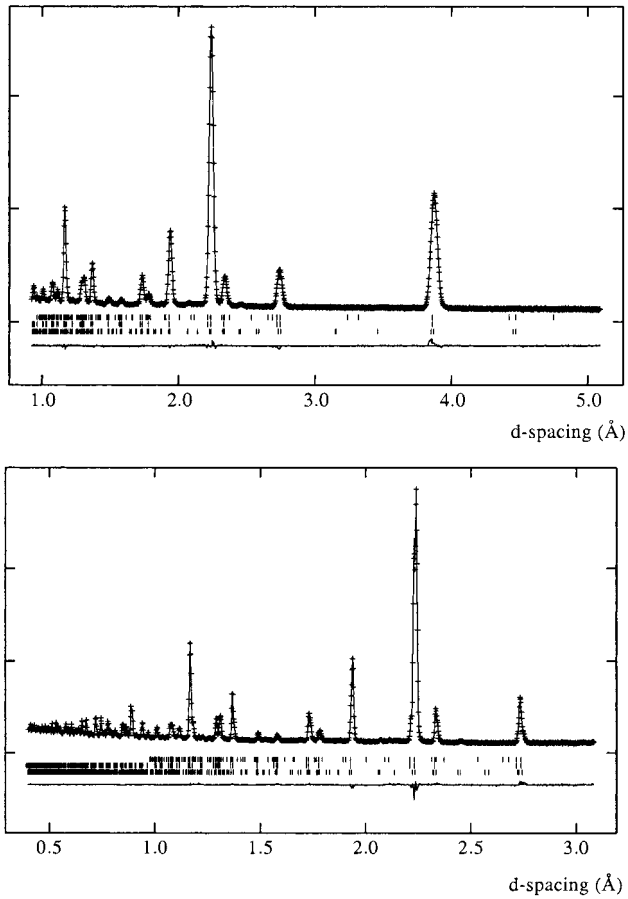

Figure 1. Rietveld fits to 4 K time-of-flight neutron powder diffraction patterns for $La_{0.7}Ca_{0.11}Sr_{0.19}MnO_3$ from the low-angle (top) and backscattering (bottom) data banks. The three sets of vertical marks correspond to the nuclear and magnetic reflections for orthorhombic *Pnma*, rhombohedral $R\bar{3}c$, and magnetic contribution for the rhombohedral phase, from bottom to top, respectively.

Quantitative analysis was carried out following the "ratio method"[26] for thin crystals where the corrections for atomic number effects, absorption, and fluorescence are negligible. In this limit, the simple expression $c_1/c_2 = k(I_1/I_2)$ can be used, where c_1 and c_2 are the weight fractions of two elements present in the specimen which give rise to intensities I_1 and I_2, respectively. The factor k can be determined from standards in which both elements are present and the compositions are known. In our case, the compositions were obtained by using the $Ln_{L\alpha}/Mn_{K\alpha}$ (Ln = La, Pr, Nd), $M_{K\alpha}/Mn_{K\alpha}$ (M = Ca, Sr), and $Ba_{L\alpha}/Mn_{K\alpha}$ ratios, and the values of k were determined from similar relations in the corresponding standards. In those samples with X-ray emission peak overlap, such as $La_{0.32}Pr_{0.38}Sr_{0.3}MnO_3$ and $Nd_{0.7}Sr_{0.16}Ba_{0.14}MnO_3$, the intensities were calculated by subtraction of minor contributions ($La_{L\beta1}$ from $Pr_{L\alpha}$ and $Ba_{L\beta2}$ from $Nd_{L\alpha}$, respectively) obtained from the appropriate ratios in the standards. More severe peak overlap of the $Mn_{K\alpha}$ with $Nd_{L\beta1}$ and $Nd_{L\beta2}$ lines occurs in $Nd_{0.7}Sr_{0.16}Ba_{0.14}MnO_3$. In this case, the intensity ratios were obtained by calculating the $Mn_{K\alpha}$ intensity from the $Mn_{K\alpha}/Mn_{K\beta}$ ratios in the standards. The results from these analyses and those from the iodometric titrations are summarized in Table 1 together with the metal−

(14) Millis, A. J.; Littlewood, P. B.; Shraiman, B. I. *Phys. Rev. Lett.* **1995**, *74*, 5144.
(15) Millis, A. J.; Shraiman, B. I.; Mueller, R. *Phys. Rev. Lett.* **1996**, *77*, 175.
(16) De Teresa, J. M.; Ibarra, M. R.; Blasco, J.; Garcia, J.; Marquina, C.; Algarabel, P. A. *Phys. Rev. B* **1996**, *54*, 1187.
(17) Ritter, C.; Radaelli, P. G.; Lees, M. R.; Barratt, J.; Balakrishnan, G.; Paul, D. Mck. *J. Solid State Chem.* **1996**, *127*, 276.
(18) Radaelli, P. G.; Marezio, M.; Hwang, H. Y.; Cheong, S.-W. *J. Solid State Chem.* **1996**, *122*, 444.
(19) Jirak, Z.; Pollert, E.; Andersen, A. F.; Grenier, J. C.; Hagenmuller, P. *Eur. J. Solid State Inorg. Chem.* **1990**, *27*, 421.
(20) Knizek, K.; Jirak, Z.; Pollert, E.; Zounova, F.; Vratislav. S. *J. Solid State Chem.* **1992**, *100*, 292.
(21) Shimura, T.; Hayashi, T.; Inaguma, Y.; Itoh, M. *J. Solid State Chem.* **1996**, *124*, 250.
(22) Radaelli, P. G.; Marezio, M.; Hwang, H. Y.; Cheong, S.-W.; Batlogg, B. *Phys. Rev. B* **1996**, *54*, 8992.
(23) Radaelli, P. G.; Iannone, G.; Marezio, M.; Hwang, H. Y.; Cheong, S.-W.; Jorgensen, J. D.; Argyriou, D. N. *Phys. Rev. B.* **1997**, *56*, 8265.
(24) Rodríguez-Martínez, L. M.; Attfield, J. P. *Phys. Rev. B.* **1998**, *58*, 2426.
(25) Larson, A. C.; von Dreele, R. B. *GSAS: General Structure Analysis System* LANSCE, MS-H805; Los Alamos National Laboratory: Los Alamos, NM 87545.
(26) Cliff, G.; Lorimer, G. W. *J. Microsc.* **1975**, *103*, 203.

Table 1. Data for $AMnO_3$ Perovskites[8] and Structural Parameters from 4 K Powder Neutron Refinements[a]

	A site			
	$La_{0.7}Ca_{0.11}Sr_{0.19}$	$La_{0.32}Pr_{0.38}Sr_{0.3}$	$Pr_{0.7}Sr_{0.23}Ba_{0.07}$	$Nd_{0.7}Sr_{0.16}Ba_{0.14}$
σ^2(Å^2)	0.0016	0.0029	0.0074	0.0123
T_m (K)	363	336	247	146
cation composition	$La_{0.70(3)}Ca_{0.09(1)}Sr_{0.20(3)}$	$La_{0.30(8)}Pr_{0.42(8)}Sr_{0.29(5)}$	$Pr_{0.74(4)}Sr_{0.22(3)}Ba_{0.08(2)}$	$Nd_{0.79(4)}Sr_{0.12(2)}Ba_{0.09(1)}$
Mn oxidation state	3.28(2)	3.26(4)	3.30(2)	3.34(4)
a (Å)	5.4586(1)	5.4544(1)	5.4602(2)	5.4680(2)
$b/\sqrt{2}$ (Å)	5.4550(1)	5.4495(1)	5.4519(1)	5.4633(2)
c (Å)	5.5005(1)	5.4953(1)	5.4848(2)	5.4800(2)
V (Å^3)	231.63(1)	231.00(1)	230.91(2)	231.52(1)
μ_{Mn} (μ_B)	3.55(1)	3.61(1)	3.55(1)	3.56(1)
μ_{Ln} (μ_B)	0	0.14(2)	0.30(1)	0.37(2)
A				
x	0.0122(2)	0.0139(1)	0.0198(2)	0.0220(1)
z	−0.0028(2)	−0.0031(2)	−0.0018(3)	−0.0039(3)
U_{iso} (Å^2)	0.00206(6)	0.00220(7)	0.0029(1)	0.0034(1)
Mn				
U_{iso} (Å^2)	0.00167(8)	0.00138(8)	0.0017(1)	0.0033(1)
O(1)				
x	0.4970(3)	0.4953(2)	0.4945(3)	0.4936(3)
z	0.0579(2)	0.0581(1)	0.0619(2)	0.0644(3)
U_{11} (Å^2)	0.0085(5)	0.0068(4)	0.0123(7)	0.0179(10)
U_{22} (Å^2)	0.0026(3)	0.0023(3)	0.0043(5)	0.0070(6)
U_{33} (Å^2)	0.0053(3)	0.0082(2)	0.0084(4)	0.0114(6)
U_{13} (Å^2)	−0.0013(4)	−0.0013(3)	−0.0026(5)	−0.0039(5)
U_{eq} (Å^2)	0.0054(4)	0.0058(3)	0.0083(6)	0.0121(7)
O(2)				
x	0.2636(2)	0.2671(1)	0.2716(2)	0.2738(2)
y	0.02929(8)	0.03020(6)	0.0307(1)	0.0308(1)
z	−0.2641(2)	−0.2669(1)	−0.2733(2)	−0.2751(2)
U_{11} (Å^2)	0.0048(3)	0.0046(2)	0.0076(4)	0.0129(5)
U_{22} (Å^2)	0.0072(2)	0.0080(2)	0.0125(3)	0.0156(4)
U_{33} (Å^2)	0.0057(3)	0.0076(2)	0.0080(4)	0.0114(4)
U_{12} (Å^2)	0.0004(2)	0.0003(2)	0.0024(3)	0.0025(4)
U_{13} (Å^2)	−0.0022(2)	−0.0022(2)	−0.0032(3)	−0.0058(3)
U_{23} (Å^2)	0.0000(3)	−0.0008(2)	−0.0016(4)	−0.0030(4)
U_{eq} (Å^2)	0.0059(2)	0.0067(2)	0.0094(3)	0.0133(4)
R_{wp} (%)	1.45	1.48	1.59	1.53
R_p (%)	2.02	1.99	2.29	2.16
χ^2	2.88	3.66	3.29	3.07

[a] The structures have orthorhombic *Pnma* symmetry with atom positions A (x, $^1/_4$, z); Mn ($^1/_2$, 0, 0); O(1) (x, $^1/_4$, z); O(2) (x, y, z).

insulator transition temperatures T_m previously reported[8] from resistivity measurements on sintered bars.

Neutron time-of-flight powder diffraction data were collected at 4 K to minimize thermal effects. These low-temperature patterns were fitted using the $GdFeO_3$ type orthorhombic $\sqrt{2}a_p \times 2a_p \times \sqrt{2}a_p$ superstructure (space group *Pnma*) of the ideal perovskite arrangement with cubic cell parameter a_p. The 4 K profile of the $La_{0.7}Ca_{0.11}Sr_{0.19}MnO_3$ composition shows the coexistence of orthorhombic *Pnma* (83%) and of rhombohedral $R\bar{3}c$ (17%) phases, as has previously been found for other compositions close to this structural boundary.[18] Figure 1 shows the Rietveld plots for this sample. The other three profiles were fitted by a single orthorhombic *Pnma* phase. Powder neutron data were fitted using a refined extinction coefficient[25] and a correction for absorption according to the analytical approximation given by Rouse and Cooper,[27] amended for cylindrical samples by Hewat.[28] The background function was fitted with a cosine Fourier series function and the peak shape was described by a convolution of two back-to-back exponentials with a pseudo-Voigt function. The atomic scattering functions reported by Watson and Freeman[29] were used to describe the angular dependence of the magnetic scattering amplitude. The ferromagnetic ordering was refined using a model of collinear Mn magnetic moments along the c axis. The same ordering model was applied to the A sites for the three samples containing magnetic lanthanides. The wide range of observed d spacings enabled the oxygen thermal factors to be refined anisotropically giving precise values for the principal mean square displacements, u_i. No deviation from full occupancy was found for any of the oxygen sites in these refinements. The refined structural parameters are listed in Table 1, and some derived quantities are shown in Table 2.

Discussion

Chemical analysis of the four $Ln_{0.7}M_{0.3}MnO_3$ samples shows that they are single phase and oxygen stoichiometric (Table 1). In the cases of $La_{0.32}Pr_{0.38}Sr_{0.3}MnO_3$ and $Nd_{0.7}Sr_{0.16}Ba_{0.14}MnO_3$ with strong X-ray emission peak overlap, the compositions obtained from EDS analysis deviate slightly from the nominal values due to systematic errors introduced in the division of

(27) Rouse, K. D.; Cooper, M. J. *Acta Crystallogr.* **1970**, *A26*, 682.
(28) Hewat, A. W. *Acta Crystallogr.* **1979**, *A35*, 248.
(29) Watson, R. E.; Freeman, A. *J. Acta Crystallogr.* **1961**, *14*, 231.

Table 2. Main Distances and Angles in $AMnO_3$ Perovskites from the 4 K Powder Neutron Refinements[a]

	A site			
	$La_{0.7}Ca_{0.11}Sr_{0.19}$	$La_{0.32}Pr_{0.38}Sr_{0.3}$	$Pr_{0.7}Sr_{0.23}Ba_{0.07}$	$Nd_{0.7}Sr_{0.16}Ba_{0.14}$
σ^2 (Å^2)	0.0016	0.0029	0.0074	0.0123
A−O distances (Å)				
A−O(1)	2.449(1)	2.448(1)	2.417(2)	2.414(2)
A−O(1)	2.667(2)	2.647(1)	2.615(2)	2.606(2)
A−O(1)	2.832(2)	2.849(1)	2.890(2)	2.914(2)
A−O(1)	3.054(1)	3.052(1)	3.075(2)	3.075(2)
A−O(2) (×2)	2.527(1)	2.506(1)	2.493(1)	2.485(1)
A−O(2) (×2)	2.617(1)	2.623(1)	2.639(1)	2.640(1)
A−O(2) (×2)	2.804(1)	2.788(1)	2.748(1)	2.744(1)
A−O(2) (×2)	3.010(1)	3.036(1)	3.081(1)	3.108(1)
mean A−O	2.743	2.742	2.743	2.747
σ^2(A−O) (Å^2)	0.039	0.043	0.052	0.057
Mn−O distances (Å)				
Mn−O(1)	1.9548(2)	1.9531(1)	1.9574(2)	1.9639(3)
Mn−O(2)	1.9507(9)	1.9538(7)	1.9498(12)	1.9535(11)
Mn−O(2)	1.9561(9)	1.9543(7)	1.9643(12)	1.9647(16)
mean Mn−O	1.9539	1.9537	1.9572	1.9607
σ^2(Mn−O) (Å^2)	0.0000051	0.0000002	0.0000350	0.0000257
angles (deg)				
Mn−O(1)−Mn	161.24(6)	161.12(4)	159.96(7)	159.19(9)
Mn−O(2)−Mn	165.29(4)	164.27(3)	162.72(5)	162.14(6)
mean Mn−O−Mn	163.94	163.22	162.72	162.14
σ^2(Mn−O−Mn)	3.47	3.31	2.54	2.90
O(1)−Mn−O(2) (×2)	90.07(4)	90.19(3)	90.21(5)	90.42(7)
O(1)−Mn−O(2) (×2)	89.93(4)	89.81(3)	89.79(5)	89.58(7)
O(1)−Mn−O(2) (×2)	89.99(4)	89.97(3)	89.85(6)	89.59(7)
O(1)−Mn−O(2) (×2)	90.01(4)	90.03(3)	90.15(6)	90.41(7)
O(2)−Mn−O(2) (×2)	91.190(5)	91.235(4)	91.055(9)	90.939(13)
O(2)−Mn−O(2) (×2)	88.810(5)	88.765(4)	88.945(9)	89.061(13)
σ^2(O−Mn−O)	0.57	0.62	0.47	0.49
ω (deg)	8.03	8.39	9.10	9.42
W	1	0.999	0.991	0.983

[a] The value of the tilt angle in the plane of the bond, ω, is obtained from the expression (180° − Mn−O−Mn angle)/2.

intensity between the overlapping peaks. The deviations in brackets given with each weight fraction correspond to the standard deviations of their distribution for the 30 crystallites analyzed which reflect the homogeneity of the sample and, in the case of $La_{0.32}Pr_{0.38}Sr_{0.3}MnO_3$, the overlap of La and Pr L lines.

The refined Mn magnetic moments are close to the ideal value of 3.7 μ_B expected for $Mn^{3.3+}$, and show no significant variation with σ^2, which rules out an increasing spin disorder as the cause of the decrease of T_m across the series. The refined crystal structures (Table 1) show systematic trends in both the long-range ordered, coherent structure (cell parameters and atomic coordinates) and the local structure (included within the temperature factors), which is disordered (incoherent) over long distances, as the cation size variance σ^2 increases. Although the unit cell volume shows no significant variation with σ^2, remaining constant to within ±0.2%, the orthorhombic distortion (evidenced by the differences between a, $b/\sqrt{2}$, and c) decreases across the series. This dependency of orthorhombicity upon σ^2 suggests that the orthorhombic−rhombohedral structural transition should also be sensitive, which is borne out by the observation of rhombohedral phase in only the first sample. However, as the remaining orthorhombic component shows a greater distortion that the other three purely orthorhombic samples, it is clear that the magnitude of the distortion is not indicative of proximity to the structural phase boundary.

The orthorhombic *Pnma* perovskite superstructure contains one A cation, one Mn site, and two crystallographically distinct oxygen positions: O(1), which gives a pair of Mn−O(1) bonds parallel to the *b* axis, and O(2) which defines two inequivalent pairs of Mn−O(2) bonds close to the ac plane (Figure 2). The coherent displacements of the A and O atoms, determined by the values of their variable atomic coordinates, all increase with increasing σ^2 (Table 1). These increase the tilting of the

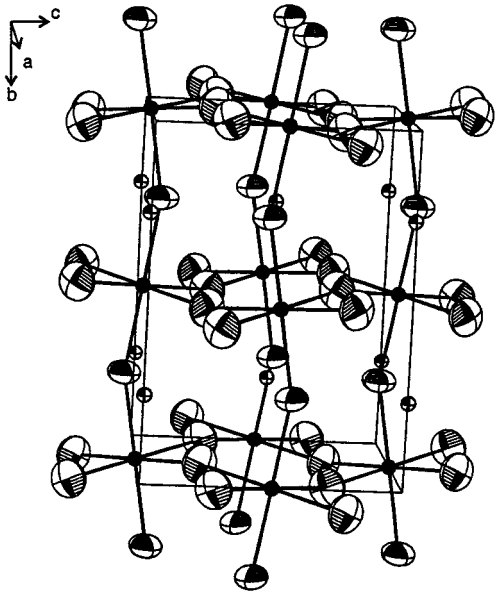

Figure 2. Schematic representation of the orthorhombic *Pnma* $AMnO_3$ structure, with the oxygen atoms represented by typical refined thermal ellipsoids (×10). The A/Mn cations thermal spheres (×50) are shaded in light/dark gray.

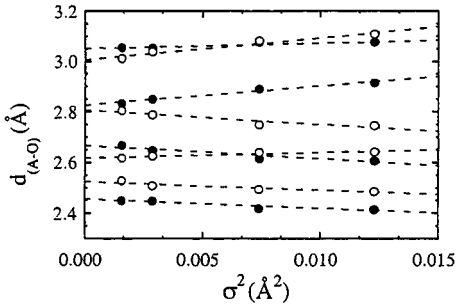

Figure 3. Variation of the A−O distances in the $AMnO_3$ perovskites with σ^2. Filled/open circles correspond to A−O(1)/O(2) distances, respectively.

MnO_6 octahedra in the ⟨001⟩ direction and their rotation around the *b* axis, although the resulting changes in the Mn−O−Mn angles are small, less than 3° across the series.

Although the orthorhombic distortion of the unit cell decreases with increasing σ^2, the distortions of the AO_{12} and MnO_6 polyhedra increase. The mean A−O distance remains constant across the series, but the individual distances all show a systematic increase or decrease such that the range, quantified by the variance in the distribution of A−O distances, σ^2(A−O) increases with σ^2 (Figure 3). A small increase in the incoherent displacements of the A cations around the mean position is evidenced by the increase in U_{iso} with σ^2, although this is a small effect in comparison with the coherent A and O atom displacements.

The coherent distortions of the MnO_6 octahedra also increase with σ^2. The slight increase of 0.007 Å in the mean Mn−O distance across the series reflects the usual anharmonicity of bonding potentials, i.e., the Mn−O bonds are more easily stretched than compressed. The variance in the distribution of Mn−O distances, σ^2 (Mn−O), which quantifies the orthorhombic distortion of the MnO_6 octahedra, generally increases with σ^2, although this is small in comparison to the increase in the incoherent Mn−O distribution evidenced below. The angular distortion of the MnO_6 octahedra, measured by the variance in the O−Mn−O distribution, shows no trend with σ^2.

Incoherent displacements of the oxygen atoms are expected to be the main consequence of increasing σ^2. The refined U_{ij} components of the anisotropic displacement tensor yield the three principal mean oxygen squared displacements, u_i, which provide information about thermal vibrations (phonons) and static disorder of these atoms around their mean positions. All three u_i's for each atom show approximately linear increases with σ^2 (Figure 4), due principally to increasing static disorder as the change in the phonon contribution at 4 K is minimal.

In the ideal cubic perovskite structure, each O atom is octahedrally coordinated by four A and two Mn cations. The close packed ionic model, described previously,[24] predicts that cation disorder only gives rise to oxygen displacements perpendicular to the Mn−O−Mn direction, (i.e., $Q_1^2 = 0$ and $Q_2^2 = Q_3^2 = \sigma^2$), giving a mean $\langle Q^2\rangle/\sigma^2 = 0.67$. The slopes u_i/σ^2 of the plots in Figure 4 give experimental measurements of the dependences of the mean squared displacements $\langle Q_i^2\rangle$ due to cation disorder. These show that all three displacements increase with σ^2, but it is notable that the mean values of $\Delta u/\sigma^2$ are 0.68 for the O(1) site and 0.63 for O(2), giving an overall weighted mean of 0.65, in excellent agreement with the predicted $\langle Q^2\rangle/\sigma^2 = 0.67$ value for the increase in mean squared oxygen displacement with A-site disorder. This verifies the use of the variance as a functional for displacive disorder of the oxygen atoms due to A cation size disorder in perovskites. It is worth noting that the individual u_i/σ^2 values are rather different from those predicted because the structures are orthorhombically distorted and so deviate significantly from the ideal cubic perovskite arrangement with $r_A^o = 1.30$ Å. At $\langle r_A\rangle = 1.23$ Å, the environment around the oxygen atoms is less symmetric than in the ideal model (Figure 4a and b), due to bending of the Mn−O−Mn angle to ∼160°.

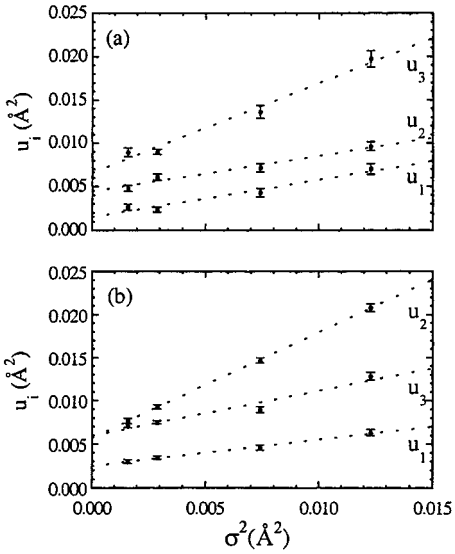

Figure 4. Variation of the principal mean squared oxygen displacements for the O(1) (a) and O(2) (b) sites.

Overall, the effects of increasing the cation size variance σ^2 within this series of four samples are found to be a decrease in orthorhombic cell distortion but an increase in coherent and incoherent atomic displacements, especially those of the oxygen atoms. The coherent oxygen displacements give rise to an increasing distortion of the AO_{12} polyhedron, which results in additional bending of the Mn−O−Mn bridges and a slight increase in the distortion of the MnO_6 octahedra. Such slight changes in average structure have previously been used to explain changes in the transition temperature T_m through reductions in the electronic bandwidth. It has previously been suggested[30] that bandwidth varies as

$$W \approx \cos \omega/d^{3.5}$$

where *d* is the mean Mn−O distance and ω is (180° − Mn−O−Mn angle)/2. Relative values of *W* calculated from this function are shown in Table 2. The change across the series is very small, a reduction of only 1.7% is calculated while T_m drops from 363 to 146 K. Furthermore this approach neglects changes in the static incoherent structure which are greater than the coherent changes of the MnO_3 framework.

(30) Medarde, M.; Mesot, J.; Lacorre, P.; Rosenkranz, S.; Fischer, P.; Gobrecht, K. *Phys. Rev. B* **1995**, *52*, 9248.

The principal mean square incoherent oxygen displacements u_2 and u_3 perpendicular to the Mn−O−Mn linkages increase markedly with σ^2, as would be expected as they are directly in line with the A−O bonds. However, an important observation (Figure 4) is that the displacements due to disorder parallel to the Mn−O−Mn direction, u_1, also increase significantly with σ^2. This displacement, unlike u_2 and u_3, moves the oxygen atom closer to one neighboring Mn than another, and so can couple to the Jahn−Teller distortions of the $Mn^{3+}O_6$ octahedra which are found in the coherently distorted parent compound $LaMnO_3$.[31] Structural studies have shown that the metal−insulator transition in $Ln_{0.7}M_{0.3}MnO_3$ perovskites is accompanied by a discontinuity in u_1 (but not in u_2 or u_3) signifying a change from dynamic to static Jahn−Teller distortions of the $Mn^{3+}O_6$ octahedra.[8,23,24] This provides an alternative explanation of the sensitivity of T_m to the structural changes in these compositions. Purely structural transitions are known to be very sensitive to small variations in structure through changes in lattice strains. A cation size mismatch leads to increasing local distortions of the MnO_6 octahedra (evidenced through u_1) which lower the strain energy required for electron localization at the metal−insulator transition, leading to a decrease in T_m. The same effect may also account for changes in T_m as the mean A cation radius decreases, which again are much greater than expected from the bandwidth changes.[23]

(31) Norby, P.; Krogh Andersen, I. G.; Krogh Andersen, E.; Andersen, N. H. *J. Solid State Chem.* **1995**, *119*, 191.

Conclusions

Changing A cation size variance while the average size and doping level are held constant results in systematic changes in both long range and local structure in this series of manganite perovskites. The major changes in coherent structure are observed in the AO_{12} coordination polyhedron. Small changes in the average Mn−O distances and Mn−O−Mn angles also occur, but these are the consequence of much larger increases in the spread of these quantities (the incoherent displacements), which do not conserve the average values due to the anharmonicity of interatomic potentials. These observations, combined with the linear dependence of T_m upon σ^2, show that local, incoherent lattice strains strongly influence the metal−insulator transition in manganite perovskites and that these effects may be more significant than bandwidth changes.

Acknowledgment. The authors acknowledge EPRSC for the provision of neutron facilities and Dr. David Jefferson, Dr. Elizabeth Tilley, and Sharon Teh for their assistance with the EDS data collection. L.M.R-M is supported by the Basque Government (Beca de Formación de Investigadores, Departamento de Educación, Universidades e Investigación).

CM980759Y